Available online at www.sciencedirect.com
ScienceDirect
Ocean Modelling 17 (2007) 153–162
Ocean Modelling
www.elsevier.com/locate/ocemod

Capturing the bottom boundary layer in finite element ocean models

Emmanuel Hanert [a,*], Eric Deleersnijder [b,c], Sébastien Blaise [d], Jean-François Remacle [d]

[a] *Department of Meteorology, The University of Reading, Earley Gate, P.O. Box 243, Reading RG6 6BB, UK*
[b] *Institut d'Astronomie et de Géophysique G. Lemaître, Université Catholique de Louvain, B-1348 Louvain-la-Neuve, Belgium*
[c] *Centre for Systems Engineering and Applied Mechanics, Université Catholique de Louvain, B-1348 Louvain-la-Neuve, Belgium*
[d] *Département de Génie Civil et Environmental, Université Catholique de Louvain, B-1348 Louvain-la-Neuve, Belgium*

Received 11 September 2006; received in revised form 27 November 2006; accepted 27 November 2006
Available online 28 December 2006

Abstract

The goal of this paper is to develop and compare numerical discretizations that explicitely take into account the logarithmic behaviour of the velocity field in the oceanic bottom boundary layer. This is achieved by discretizing the governing equations by means of the finite element method and either enriching or modifying the set of shape functions used to approximate the velocity field. The first approach is based on the extended finite element formalism and requires additional "enriched" degrees of freedom near the bottom. The second approach amounts to using logarithmic shape functions in the bottom element instead of the usual linear ones. Both approaches are compared with analytical and classical finite element solutions in the case of rotating and non-rotating bottom boundary layer flows.

Keywords: Bottom boundary layer; Enriched finite element methods

1. Introduction

Most current ocean and coastal circulation models use a non-constant vertical eddy viscosity profile to take into account the variations of turbulent mixing with depth. The latter is influenced by shear and stratification and varies considerably over the depth of the ocean. Near the ocean bottom, shearing effects are dominant and eddy viscosity is generally parametrized as a linear function of the distance to the bottom (Ellison, 1956; Weatherly and Martin, 1978). Such a behaviour leads to a logarithmic velocity profile just above the bottom whose height depends on the roughness of the bottom. The typical height of the logarithmic bottom boundary layer (BBL) is generally much smaller than the vertical resolution available in a 3D ocean circulation model (Weatherly and Martin, 1978).

* Corresponding author.
E-mail address: e.a.hanert@reading.ac.uk (E. Hanert).

1463-5003/$ - see front matter
doi:10.1016/j.ocemod.2006.11.006

Therefore, most grid point finite difference models do not explicitely resolve the BBL. Instead, they take its impact into account by resorting to "law of the wall" approaches (e.g. Rodi, 1993), the most popular of which consists in estimating the bottom stress as a quadratic function of the velocity that is computed above the sea bed (e.g. Blumberg and Mellor, 1987; Deleersnijder et al., 1992; Davies et al., 1995). This technique is consistent with the logarithmic layer theory provided the first grid point above the bottom boundary is located in the logarithmic layer (Tennekes, 1973).

Here, we would like to evaluate some finite element discretizations of the BBL and see how accurately they can represent the velocity profile. Unlike the finite difference method, the finite element method (FEM) allows a greater flexibility in both the geometrical discretization of the computational domain and in the functional discretization of the model variables. Geometrical flexibility is achieved thanks to the use of unstructured meshes that accurately represent complex domains and allow for local mesh refinement (Goreman et al., 2006; Legrand et al., 2006). This has been extensively used to simulate 2D horizontal and 3D oceanic and shallow-water flows (e.g. Lynch et al., 1996; Danilov et al., 2004; Hanert et al., 2005; Pain et al., 2005; Walters, 2006; White and Deleersnijder, in press). By functional flexibility, we mean the ability to locally change the type of shape functions used to approximate the model variables. This feature has been less used for oceanic applications except in some recent studies on the use of p-adaptive Discontinuous Galerkin methods to simulate shallow water flows.

Functional flexibility has been used to a greater extent for some engineering applications where the classical FEM fails or is prohibitively expensive. This is typically the case for problems with rough coefficients, boundary layers or highly oscillatory solutions. The main idea behind this improved FEM, usually called Partition of Unity FEM (PUFEM) or eXtended-FEM (X-FEM) (Melenk and Babuška, 1996; Babuška and Melenk, 1997; Moës et al., 1999), is to design the shape and test functions in view of the problem under consideration. Hence if the analytic behaviour of the solution is available, the approximation of the solution can be improved by taking this information into account. In contrast to that, the classical FEM has to use very small mesh sizes in order to deal with the singular behaviour of the solution.

In this work, we are going to deal with the particular issue of the oceanic BBL and try to apply some of the above-mentioned techniques to build finite element scheme that accurately represent the velocity field in the BBL. The model equations are presented in Section 2 and their analytical solutions is derived in Section 3. Finite element discretizations designed to capture the BBL are introduced in Section 4. These discretizations follow or are inspired by the X-FEM formalism. Finally, a numerical evaluation of the suggested schemes is performed in Section 5.

2. Model equations

For the sake of simplicity, it is assumed that the flow near the bottom is horizontally homogeneous and only depends on Coriolis, pressure gradient and vertical friction forces. We thus neglect time derivatives, advection terms and horizontal diffusion. These assumptions are realistic in the vicinity of the ocean bottom. Moreover, we are also going to assume that above the BBL, the flow is in geostrophic balance and the pressure gradient is depth-independent.

In that case, the problem reduces to seeking the horizontal velocity $\mathbf{u}(z) = (u(z), v(z))$ that satisfies the following equation:

$$f(\mathbf{u} - \mathbf{u}_g) \times \mathbf{e}_z = \frac{d}{dz}\left(\nu \frac{d\mathbf{u}}{dz}\right), \tag{1}$$

where $z \in [0, L]$ is the vertical coordinate, f is the Coriolis parameter, $\mathbf{u}_g = (u_g, v_g)$ is the geostrophic velocity, ν is the kinematic eddy viscosity and $\mathbf{e}_z$ is a unit vector pointing upward.

In the sheared boundary layer, a classical parametrization of the eddy viscosity is

$$\nu(z) = \kappa u_* z,$$

where $\kappa = 0.41$ is the von Kàrman constant and u_* is the friction velocity (Ellison, 1956). The friction velocity can be expressed in terms of the bottom stress $\boldsymbol{\tau}$ as $u_* = \sqrt{\|\boldsymbol{\tau}\|_2/\rho}$, where ρ is the fluid's density.

The solution of Eq. (1) should satisfy a no-slip boundary condition at the bottom. However, as it is not possible to represent accurately the flow below the roughness height (z_0), it is generally assumed that the horizontal velocity vanishes at the level $z = z_0$ rather than at the bottom level $z = 0$. We may then redefine the vertical coordinate as $z = z - z_0$. In that case, the turbulent viscosity becomes $\nu = \kappa u_*(z + z_0)$ and the no-slip boundary condition simply reads

$$\mathbf{u}(z = 0) = 0. \tag{2}$$

Another boundary condition amounts to imposing the momentum flux at the bottom.

$$\left[\rho\nu\frac{\mathrm{d}\mathbf{u}}{\mathrm{d}z}\right]_{z=0} = \boldsymbol{\tau}. \tag{3}$$

The bottom stress $\boldsymbol{\tau} \equiv \tau\mathbf{e}_\tau = \rho u_*^2\mathbf{e}_\tau$ is applied in the direction $\mathbf{e}_\tau$. We can also define the perpendicular direction $\mathbf{e}_\perp = (\mathbf{e}_\tau \times \mathbf{e}_z)\mathrm{sign}(f)$.

3. Velocity profile in the BBL

To compute the exact solution of Eq. (1), we arbitrarily impose the value of the friction velocity. The latter is generally not imposed in practice as it depends on the magnitude of the bottom stress, which in turn is proportional to the velocity gradient via (3). We make this approximation in order to be able to find a simple – and easy to deal with – analytical solution to Eq. (1) without having to solve a nonlinear problem. Moreover, the value of the geostrophic velocity is chosen in such a way that the velocity satisfies boundary conditions (2), (3) and reduces to the geostrophic velocity faraway from the bottom. The same approach has been followed by Ellison (1956), who first derived an analytical solution for velocity in a rotating BBL.

The solution of Eq. (1) may be reduced to a scalar problem by introducing the complex velocities $w = (\mathbf{u} - \mathbf{u}_\mathrm{g}) \cdot \mathbf{e}_\perp + \mathrm{i}(\mathbf{u} - \mathbf{u}_\mathrm{g}) \cdot \mathbf{e}_\tau$ and $w_\mathrm{g} = \mathbf{u}_\mathrm{g} \cdot \mathbf{e}_\perp + \mathrm{i}\mathbf{u}_\mathrm{g} \cdot \mathbf{e}_\tau$. The imaginary part of w represents the component of $(\mathbf{u} - \mathbf{u}_\mathrm{g})$ parallel to the bottom stress, while its real part is orthogonal to the bottom stress. Eq. (1) can then be expressed as

$$\frac{\mathrm{d}}{\mathrm{d}z}\left(\nu(z)\frac{\mathrm{d}w}{\mathrm{d}z}\right) = \mathrm{i}|f|w, \tag{4}$$

where w and w_g should satisfy the following conditions:

$$w(0) = -w_\mathrm{g}, \tag{5}$$

$$\left[\rho\nu(z)\frac{\mathrm{d}w}{\mathrm{d}z}\right]_{z=0} = \mathrm{i}\tau, \tag{6}$$

$$\lim_{z\to\infty} w(z) = 0. \tag{7}$$

By introducing $\xi = 2\mathrm{e}^{\mathrm{i}\pi/4}\sqrt{\frac{(z+z_0)|f|}{\kappa u_*}}$, we may rewrite Eq. (4) as

$$\frac{\mathrm{d}^2w}{\mathrm{d}\xi^2} + \frac{1}{\xi}\frac{\mathrm{d}w}{\mathrm{d}\xi} - w = 0 \tag{8}$$

of which the solution that satisfies (7) is

$$w(\xi) = AK_0(\xi),$$

where K_0 is the 0th order modified Bessel function of the second kind. The integration constant A is found by imposing boundary condition (6). The final velocity solution reads

$$w(\xi) = -2\mathrm{i}\frac{u_*}{\kappa}\frac{K_0(\xi)}{\xi_0 K_1(\xi_0)}, \tag{9}$$

where $\xi_0 = 2\mathrm{e}^{\mathrm{i}\pi/4}\sqrt{\frac{z_0|f|}{\kappa u_*}}$ and $K_1 = -K_0'$ is the 1st order modified Bessel function of the second kind. It should be noted that the solution of Eq. (4) is often expressed in terms of Kelvin or Hankel functions rather than Bessel functions (e.g. Ellison, 1956; Cushman-Roisin and Malačič, 1997). Finally, the geostrophic velocity is found from (5): $w_g = -w(\xi = \xi_0)$.

The length scale $\kappa u_*/|f|$, called here the Coriolis length, represents the distance from the bottom at which the veering of the velocity due to the Coriolis force becomes important. For $z \ll \kappa u_*/|f|$, rotational effects are small and the velocity profile is expected to be logarithmic. This is confirmed by computing the asymptotic velocity solution when $\xi \to 0$. The K_0 and K_1 Bessel functions asymptotically behave like $-\log(\xi)$ and $1/\xi$, respectively (Abramowitz and Stegun, 1965) and (9) therefore reduces to

$$w(z) + w_g \sim \frac{u_*}{\kappa} \mathrm{i} \log\left(1 + \frac{z}{z_0}\right), \quad \text{for } z \to 0.$$

This is the usual logarithmic velocity profile in a turbulent boundary layer in the absence of rotation:

$$\mathbf{u}(z) = \frac{u_*}{\kappa} \log\left(1 + \frac{z}{z_0}\right)\mathbf{e}_\tau. \tag{10}$$

The asymptotic solution has the same orientation as the bottom stress and therefore does not represent the veering of the velocity due to rotation. It should be noted that small values of ξ are only possible if ξ_0 is also small as $|\xi| \geqslant |\xi_0|$, which is generally the case in practice.

4. Finite element discretization

In this section, we present three finite element approximations to the exact solution of Eq. (1).

The first approach is the classical linear finite element approximation, which amounts to approximating the exact solution as:

$$\mathbf{u}(z) \approx \mathbf{u}^h_{P_1}(z) = \sum_{i=1}^{N} \mathbf{u}_i \phi_i(z), \tag{11}$$

where $\phi_i(z)$ is the piecewise linear P_1 shape function associated with node i (see Fig. 1) and N is the number of vertices in the 1D grid or mesh.[1] This approximation yields a quadratic convergence rate in the L_2-norm if the finite element grid is able to represent the boundary layer. If this is not the case, poor convergence is expected.

In order to avoid poor rates of convergence, the extended finite element method (X-FEM) has been introduced. This method amounts to locally enriching the classical finite element approximation (11) in a way that takes the exact behaviour of the solution into account. This approximation, denoted $X - P_1$, reads:

$$\mathbf{u}(z) \approx \mathbf{u}^h_{X-P_1}(z) = \mathbf{u}^h_{P_1}(z) + \mathbf{u}^h_{\mathrm{enr}}(z), \tag{12}$$

where $\mathbf{u}^h_{P_1}(z)$ is given by (11) and $\mathbf{u}^h_{\mathrm{enr}}(z)$ reads

$$\mathbf{u}^h_{\mathrm{enr}}(z) = \sum_{j=1}^{M} \mathbf{b}_j \phi_j(z) F(z). \tag{13}$$

The additional degrees of freedom $\mathbf{b}_j$ are added to the nodes whose support lies in the BBL. As the grid size is usually much larger than the BBL height, additional degrees of freedom are limited to the bottommost element. The function F is called the enrichment function (Moës et al., 1999) and allows us to incorporate our knowledge of the exact solution directly into the finite element space. As we know that $\mathbf{u}(z)$ reduces to (10) in the BBL, we define the enrichment function as

$$F(z) = \log\left(1 + \frac{z}{z_0}\right).$$

The resulting additional shape functions $\phi^X_j(z) \equiv \phi_j(z)F(z)$ are shown in Fig. 1.

[1] Note that in a 1D problem, both mesh and grid mean the partition of the domain into non-overlapping elements. This partition will always be structured although the size of the elements may change. By vertices, we mean the nodes lying on elements extremities.

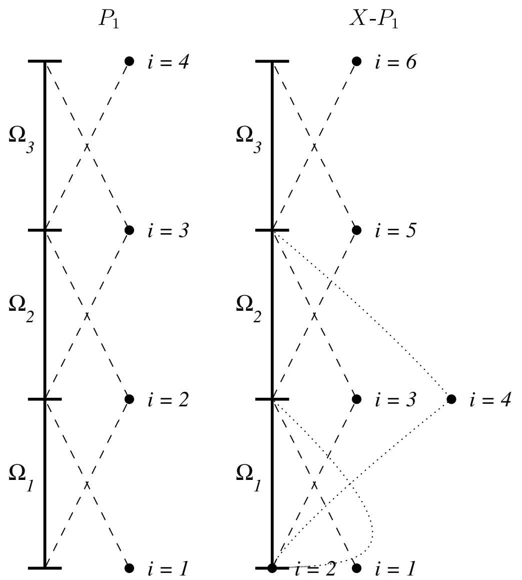

Fig. 1. Sketch of the first three elements of the 1D finite element grid for the classical P_1 scheme (left), the $X - P_1$ scheme (center) and the $\log - P_1$ scheme (right). The two additional shape functions used in the $X - P_1$ scheme are represented with a dotted line.

A third approach amounts to using logarithmic shape functions in the bottom element *instead* of the P_1 shape functions to mimic the behaviour of the exact solution. Hence, the following approximation, denoted $\log - P_1$, is used:

$$\mathbf{u}(z) \approx \mathbf{u}^h_{\log - P_1}(z) = \sum_{i=1}^{N} \mathbf{u}_i \psi_i(z), \tag{14}$$

where the shape functions $\psi_i(z)$ are defined as:

$$\psi_1(z) = 1 - \psi_2(z), \tag{15}$$

$$\psi_2(z) = \log\left(1 + \frac{z}{z_0}\right) \Big/ \log\left(1 + \frac{d}{z_0}\right), \tag{16}$$

$$\psi_i(z) = \phi_i(z) \quad \text{for } i = 3, \ldots, N, \tag{17}$$

where d is the height of the bottommost element of the grid (i.e. $\Omega_1 = [0, d]$, see Fig. 1). With this approach, the logarithmic shape functions (15) and (16) are used in place of P_1 shape functions in Ω_1. Their "shape" depends on the ratio between the element size d and the roughness height z_0 (Fig. 2) and they reduce to P_1 shape functions when the grid is fine enough to represent the BBL, i.e. when $d \lesssim z_0$. The use of these shape functions in the bottom element does not change the number of degrees of freedom.

One may argue that shape functions inspired by the velocity solution in a rotating BBL would be more accurate than the logarithmic shape functions proposed here. Using (9) to build shape functions is however not straightforward as the argument of the Bessel function K_0, ξ, depends on the friction velocity u_*. The latter is generally unknown and has to be expressed in terms of the velocity near the bottom. Hence, velocity shape

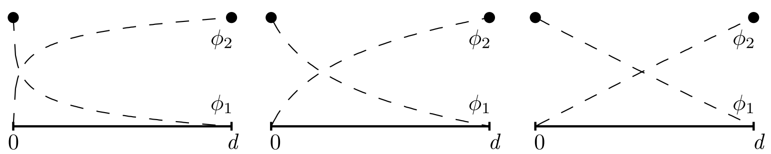

Fig. 2. Logarithmic shape functions used in the bottom element. The ratio z_0/d is equal to 10^{-3}, 10^{-1} and 10 (from left to right).

functions would depend on the velocity, which might not be desirable in practice. Adding one more term to the asymptotic development of $K_0(\xi)$ also leads to complex expressions that depend on the friction velocity.

We refer to Hanert et al. (2006) for details on the way to derive the discrete equations once the finite element approximation has been defined. We shall just mention that the Galerkin procedure is used for the P_1 and $X-P_1$ schemes while a Petrov–Galerkin procedure is used for the $\log{-P_1}$ scheme. The former amounts to using test functions identical to shape functions while the latter allows to use test functions that are different from the shape functions. In the case of the $\log{-P_1}$ scheme, P_1 test functions are used all over the domain (i.e. even in the bottom element). This allows us to have smoother functions to integrate. The numerical integration order and the computational cost are thus reduced.

5. Numerical simulations and discussions

Let us now try to assess and compare the numerical schemes introduced in the previous section. Numerical results are compared to the analytical velocity solutions (10) and (9) obtained for a non-rotating and rotating BBL, respectively. The numerical domain is 100 m high and is discretized with different uniform grids, whose resolution goes from 50 to 0.1 m. The model resolution could of course be locally increased near the bottom but even then it would be hard to match the resolution required to explicitly represent the BBL. Moreover in a realistic model, this would lead to a very severe stability condition on the time step. The model parameters have the following values: $f = 0$ or $10^{-4}\ \mathrm{s}^{-1}$, $\rho = 1010\ \mathrm{kg\ m}^{-3}$, $z_0 = 10^{-3}$ m and $u_* = 10^{-2}\ \mathrm{m\ s}^{-1}$. The bottom stress is applied in the direction $\mathbf{e}_\tau = (1/\sqrt{2}, 1/\sqrt{2})$.

As boundary conditions, the value of the analytical solution is imposed at the top and at the bottom of the domain. The latter amounts to the no-slip boundary condition (2). We also consider a free-slip boundary condition at the bottom as this kind of condition is often used in practice. In that case, condition (3) is used instead of (2) at the bottom. However, a free-slip condition is only used for the P_1 scheme as the two others ($X-P_1$ and $\log{-P_1}$) are specially designed to deal with the no-slip bottom boundary condition.

Fig. 3 shows the analytical and numerical velocity solutions in the non-rotating BBL obtained for grid sizes of 5 and 20 m. The grid is obviously too coarse to represent the BBL. As expected, a fully linear approximation of the velocity with a no-slip boundary condition gives a very poor velocity profile in the BBL and in the rest of the domain as well. The velocity value at the bottom might be correct but the above solution largely under-estimates the exact velocity. Better results are obtained when using a free-slip boundary condition as the numerical solution is now very close to the exact solution everywhere except in the BBL where the exact velocity is over-estimated. The use of the boundary condition (3) instead of (2) amounts to imposing the correct bottom stress rather than the correct velocity value. The solution in most of the domain is therefore fine except near the bottom where it cannot vanish while still giving the right stress. This problem does not occur with the $X-P_1$ and $\log - P_1$ schemes as these explicitely take into account the logarithmic behaviour of the velocity in the BBL. Both schemes are working equally well and give solutions almost identical to the exact solution.

In the general rotating case (Fig. 4), the P_1 scheme behaves the same as before. However, results obtained with the $\log - P_1$ scheme are now less accurate as the shape functions used in the bottom element do not exactly mimic the analytical solution anymore. In particular, the logarithmic shape functions do not take the veering of the velocity into account. The numerical solution is thus less accurate when the grid size is not small compared to the Coriolis length, equal to about 40 m in this experiment. In this case, the $X-P_1$ scheme is working better as P_1 degrees of freedom are still present in the bottom element. These nodes can account for the veering effect and the solution is thus qualitatively better.

A more quantitative evaluation can be achieved by computing the L_2 relative error between the exact and numerical solutions. The latter is defined as $\mathrm{e} = \frac{\int_\Omega (u_\mathrm{h} - u_\mathrm{ex})^2 \mathrm{d}\Omega}{\int_\Omega u_\mathrm{ex}^2 \mathrm{d}\Omega}$, where u_h and u_ex denote the discrete and exact solutions, respectively. Fig. 5 shows the behaviour of the error for grid sizes going from 0.1 m to 50 m. A grid size of 0.1 m is obviously unaffordable in any realistic 3D model. However, locally increasing the resolution to achieve a 5 m grid size near the bottom while having a much coarser resolution in the mid-ocean is achievable. For all schemes, the error is decreasing quite slowly for grid sizes larger than about 1 m. For grid sizes smaller than that, convergence is more rapid although not quadratic. The expected quadratic convergence rate should only be achieved for grid sizes of the order of $z_0 = 10^{-3}$ m.

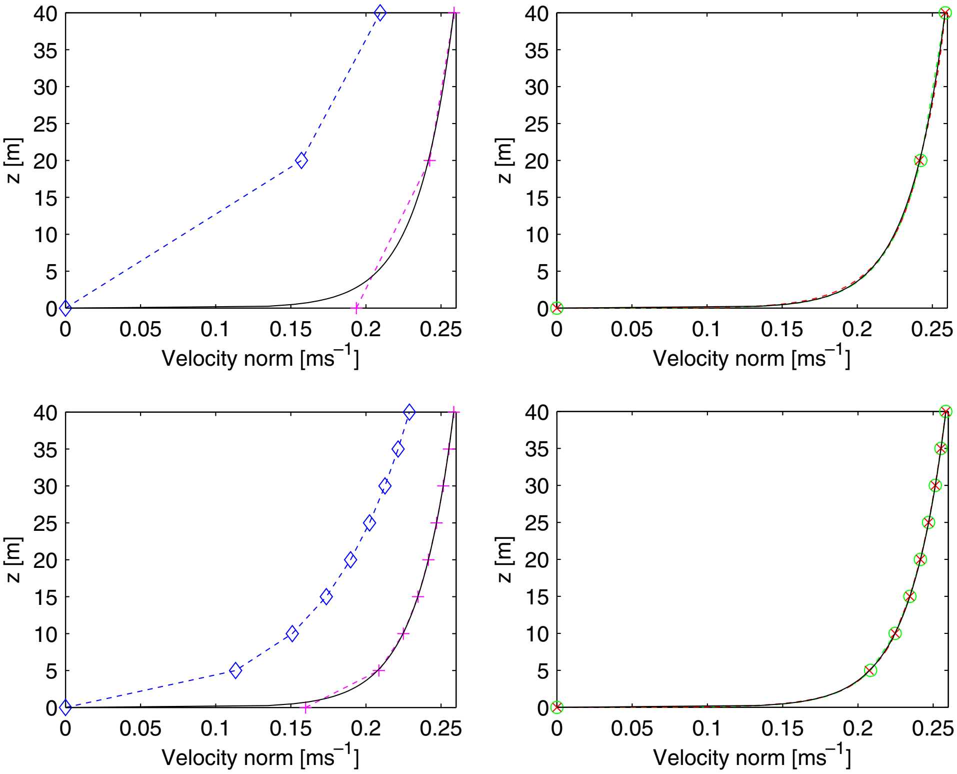

Fig. 3. Snapshot of the velocity profile in the non-rotating BBL ($f = 0$) obtained with different finite element discretizations (dashed lines) versus the analytical solution (solid line). The grid resolution is set to 20 m (top) and 5 m (bottom). Results obtained with the P_1 scheme are shown on the left and those obtained with the $\log - P_1$ and $X - P_1$ schemes are shown on the right. The symbols "◇", "+", "○" and "×" represent the nodal values of the no-slip P_1, free-slip P_1, $\log - P_1$ and $X - P_1$ discrete solutions, respectively. Note that the $\log - P_1$ and $X - P_1$ solutions are almost identical to the exact solution.

In the non-rotational case, large differences are observed between the different schemes. For the classical P_1 schemes, the use of free-slip boundary conditions reduces the error by about one order of magnitude. The error is further reduces by one order of magnitude when using the $\log - P_1$ scheme. Finally, the $X - P_1$ scheme is working best with numerical errors of the order of 10^{-5}. The same trends are observed in the rotational case, except that now the $\log - P_1$ scheme is only performing better than the P_1 scheme with free-slip boundary condition for grid sizes smaller than the Coriolis length. Again, this result was expected as the $\log - P_1$ scheme is designed specifically for a non-rotating BBL and does not take veering into account. The $X - P_1$ scheme is more general than in the sense that all the P_1 degrees of freedom are preserved and additional nodes are used in the bottommost element to handle the logarithmic boundary layer. As a result, the $X - P_1$ scheme performs equally well in the rotational and non-rotational cases for all resolutions.

For P_1 schemes, the poor rate of convergence is due to the lack of resolution in the BBL. One could however wonder why a better convergence rate is not obtained with the $\log - P_1$ scheme, in the non-rotational case at least. Indeed errors are much smaller in that case but the error curve is not steeper. This is due to the fact that logarithmic shape functions are only used in the bottommost element. The numerical error in that element is therefore very small. As resolution increases, the size of that element decreases and the proportion of the domain where P_1 shape functions are used increases. As a result, the error in the bottom of the domain might increase. For instance, if the bottom element is divided into two new elements, the finite element approximation will be logarithmic in the first element but only linear in the second one. The error in the two bottom elements, taken as a whole, might thus increase compared to the error in the previous bottom element. This is likely to upset the convergence rate. The same error behaviour is also observed for the $X - P_1$ scheme as the enriched degrees of freedom are limited to the bottommost element.

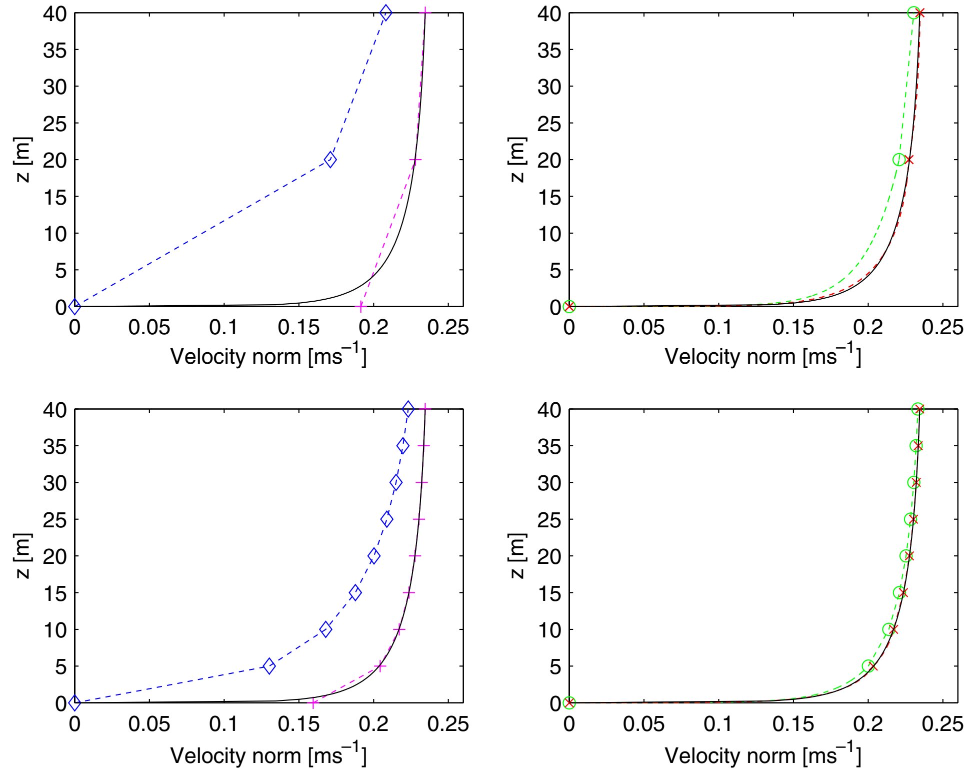

Fig. 4. Same as Fig. 3 but for a rotating BBL ($f = 10^{-4}\,\mathrm{s}^{-1}$). Note that the $X - P_1$ solution is still almost identical to the exact solution while the $\log - P_1$ solution is less accurate than in the non-rotating case.

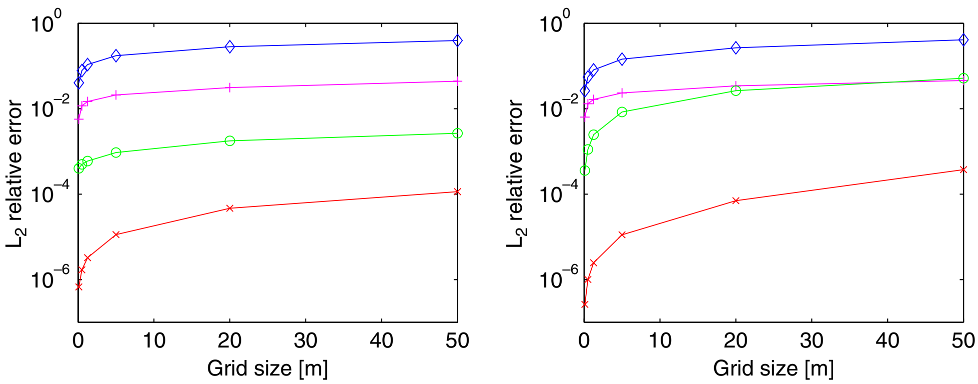

Fig. 5. L_2 relative error between the analytical and discrete solutions in the case of a non-rotating (left) and rotating (right) BBL flow for different grid sizes. The no-slip P_1, free-slip P_1, $\log - P_1$ and $X - P_1$ solutions are represented by"◇", "+", "○" and "×" symbols, respectively.

Finally, it is worth noting that the $X - P_1$ scheme might be weaker than the other schemes in terms of computational efficiency. Indeed, when writing the discrete equations in matrix form $Ax = b$, the matrix A is tridiagonal when P_1 and $\log - P_1$ schemes are used. This is however not the case with the $X - P_1$ scheme as there are 4 degrees of freedom in the bottommost element instead of 2 for the other schemes. This could make the efficient implementation of the $X - P_1$ scheme more difficult as it prevents the use of a tridiagonal solver. Moreover, the numerical integration order required to accurately integrate products of shape and test functions or their derivatives is low in the case of classical P_1 and $\log - P_1$ schemes. This is not the case for the

$X - P_1$ scheme, where a large number of Gauss integration points (about 30) is required in the enriched elements. This problem often occurs with extended FEM's and was already mentioned in the seminal paper of Melenk and Babuška (1996).

6. Conclusion

Two finite element schemes, denoted $X - P_1$ and $\log - P_1$, have been proposed to solve the velocity field in the oceanic BBL. The common idea of these schemes is to explicitely take into account the logarithmic behaviour of the velocity in the BBL. For the $X - P_1$ scheme, this is achieved by enriching a classical P_1 finite element approximation with additional degrees of freedom near the bottom. The $\log - P_1$ scheme is more specific as it amounts to replacing P_1 shape functions by logarithmic shape functions in the bottom element. The logarithmic shape functions exactly mimic the velocity profile near the ocean bottom, where rotation effects are negligible.

The $X - P_1$ scheme is more general in the sense that it preserves all the P_1 nodes and adds some new nodes to reproduce the logarithmic behaviour. The main advantage of the $X - P_1$ scheme over the more specific $\log - P_1$ scheme is that it works equally well when rotational effects are not negligible. In that case, the velocity undergoes some veering and deviates from the logarithmic solution. The $\log - P_1$ scheme is not able to represent that deviation and is thus less accurate. However, despite those shortcomings, the $\log - P_1$ scheme is interesting for small-scale applications, where rotational effects are negligible, or when the grid size is fine enough. This is mainly due to the simplicity of that scheme that renders it more efficient and computationally cheaper.

Acknowledgements

E.H. thanks the Nuffield Foundation for a newly appointed lecturer award. E.D. is Research Associate with the Belgian National Fund for Scientific Research (FNRS). E.D., S.B. and J.F.R. carried out this study within the scope of the project "A second-generation model of the ocean system", which is funded by the *Communauté Française de Belgique*, as *Actions de Recherche Concertées*, under the contract ARC 04/09-316.

References

Abramowitz, M., Stegun, I.A., 1965. Handbook of Mathematical Functions. Dover Publications, New York.

Babuška, I., Melenk, J.M., 1997. The partition of unity method. International Journal for Numerical Methods in Engineering 40, 727–758.

Blumberg, A.F., Mellor, G.L., 1987. A description of a three-dimensional coastal ocean circulation model. In: Heaps, N.S. (Ed.), Three Dimensional Ocean Models, . In: Coastal and Estuarine Sciences. American Geophysical Union, Washington, DC, pp. 1–16.

Cushman-Roisin, B., Malačič, V., 1997. Bottom Ekman pumping with stress-dependent eddy viscosity. Journal of Physical Oceanography 27, 1967–1975.

Danilov, S., Kivman, G., Schröter, J., 2004. A finite element ocean model: principles and evaluation. Ocean Modelling 6, 125–150.

Davies, A.M., Luyten, P.J., Deleersnijder, E., 1995. Turbulence energy models in shallow sea oceanography. In: Lynch, D.R., Davies, A.M. (Eds.), Quantitative Skill Assessment for Coastal Ocean Models, . In: Coastal and Estuarine Studies, vol. 47. AGU, Washington, DC, pp. 97–123.

Deleersnijder, E., Norro, A., Wolanski, E., 1992. A three-dimensional model of the water circulation around an island in shallow water. Continental Shelf Research 12, 891–906.

Ellison, T.H., 1956. Atmospheric turbulence. In: Batchelor, G.K., Da vies, R.M. (Eds.), Surveys in Mechanics, In: G.I. Taylor Anniversary Volume, vol. 4. Cambridge University Press, pp. 400–430.

Goreman, G.J., Piggott, M.D., Pain, C.C., de Oliveira, C.R.E., Umpleby, A.P., Goddard, A.J.H., 2006. Optimisation based bathymetry approximation through constrained unstructured mesh adaptivity. Ocean Modelling 12, 436–452.

Hanert, E., Le Roux, D.Y., Legat, V., Deleersnijder, E., 2005. An efficient Eulerian finite element method for the shallow water equations. Ocean Modelling 10, 115–136.

Hanert, E., Deleersnijder, E., Legat, V., 2006. An adaptive finite element water column model using the Mellor-Yamada level 2.5 turbulence closure scheme. Ocean Modelling 12, 205–223.

Legrand, S., Deleersnijder, E., Hanert, E., Legat, V., Wolanski, E., 2006. High-resolution, unstructured meshes for hydrodynamic models of the Great Barrier Reef, Australia. Estuarine, Coastal and Shelf Science 68, 36–46.

Lynch, D.R., Ip, J.T.C., Naimie, C.E., Werner, F.E., 1996. Comprehensive coastal circulation model with application to the Gulf of Maine. Continental Shelf Research 16, 875–906.

Melenk, J.M., Babuška, I., 1996. The partition of unity finite element method: Basic theory and applications. Computer Methods in Applied Mechanics and Engineering 139, 289–314.
Moës, N., Dolbow, J., Belytschko, T., 1999. A finite element method for crack growth without remeshing. International Journal for Numerical Methods in Engineering 46, 131–150.
Pain, C.C., Piggott, M.D., Goddard, A.J.H., Fang, F., Goreman, G.J., Marshall, D.P., Eaton, M.D., Power, P.W., de Oliveira, C.R.E., 2005. Fully three-dimensional unstructured mesh ocean modelling. Ocean Modelling 10, 5–33.
Rodi, W., 1993. Turbulence Models and their Applications in Hydraulics: A State-of-the-Art Review. A.A. Balkema, Rotterdam.
Tennekes, H., 1973. The logarithmic wind profile. Journal of the Atmospheric Sciences 30, 234–238.
Walters, R.A., 2006. Design considerations for a finite element coastal ocean model. Ocean Modelling 15, 90–100.
Weatherly, G.L., Martin, P.J., 1978. On the structure and dynamics of the oceanic bottom boundary layer. Journal of Physical Oceanography 8, 557–570.
White, L., Deleersnijder, E., Diagnoses of vertical transport in a three-dimensional finite element model of the tidal circulation around an island. Estuarine, Coastal and Shelf Science, in press.